Supporting Information

Hur et al. 10.1073/pnas.1207326109

SI Text

SI Materials and Methods. ***Preparation of substrates.*** Deformable polyacrylamide (PAA) substrate was prepared as previously described in detail (1). Materials were purchased from Bio-Rad (Bio-Rad Laboratories Inc., Hercules, CA) unless otherwise mentioned. In brief, the acrylamide/bis-acrylamide solution was prepared with acrylamide, N,N'-methylene bis-acrylamide, Hepes buffer, and distilled water, with a final concentration of acrylamide/Bis = 5%/0.1%. To this, 0.04% (or 9.1×10^{10} per mL) of 0.2-μm diameter red fluorescent (580/605) polystyrene beads (Invitrogen, Carlsbad, CA), 0.06% ammonium persulfate (APS, Sigma), and 0.4% N,N,N',N'-tetramethylene diamine (TEMED, Invitrogen) were added. The distance between beads is approximately 2.2 μm. The solution was spread as a sheet on the activated 35 × 60 mm glass coverslip (Fisher, Pittsburgh, PA) and allowed to polymerize for 40 min at room temperature.

The Young's Modulus of the substrate determined with atomic force microscopy was 3.63 kPa. The mechanical properties (including elasticity) of PAA were tested in previous studies (1). The value of 0.3 was used as the Poisson's ratio, as measured in a previous study (2). The surface of the polyacrylamide gel was coated with fibronectin (FN, 100 μg/mL; Sigma-Aldrich Co., St. Louis, MO) as the substratum for EC culture.

Cell culture. Cell culture reagents were purchased from Invitrogen (Invitrogen Corp., Carlsbad, CA) unless otherwise mentioned. Bovine aortic endothelial cells (ECs, VEC Technologies Inc., Rensselaer, NY) were cultured in a 10-cm Petri dish containing Dulbecco's modified Eagle's medium (DMEM) supplemented with 10% FBS, 1% sodium pyruvate, 1% L-glutamine, and 1% penicillin-streptomycin. The culture was maintained in a humidified 5% CO_2/95% air incubator at 37 °C. Experiments were conducted with cells before passage 15.

Live-cell imaging. ECs were seeded onto PAA substrate, and a spinning disk confocal microscope (IX-81, Olympus America Inc., Center Valley, PA) with a 60 × objective lens (UIS Plan-Apo, N.A. 1.40, Olympus) was used to track the movement of the embedded red fluorescent (580/605) beads (fluorescence mode) and ECs (DIC mode) in Z as well as X and Y directions. The magnification scale was 0.1075 μm/pixel in X and Y directions, and the optical section step in Z direction was 0.2 μm. Force-loaded images were acquired from the bead-embedded gel on which ECs were attached and exerted their traction force. The null-force images were taken from the gel without the ECs following their removal with trypsin-EDTA (Sigma) to eliminate the cell-induced gel deformation. Displacements were determined by dividing each 3D force-loaded image and comparing it with corresponding null-force image in 3D interrogation boxes, similar to our previous study (3). We then calculated the correlation function between pairs of boxes and found the displacement that maximizes the correlation. This process did not require image deconvolution algorithms.

Shear stress experiment. A recirculating flow system was used to impose laminar and oscillatory flow shears to ECs cultured on PAA substrate (4–7). In brief, a 35 × 60 mm glass slide with a confluent EC monolayer cultured on PAA was mounted in a rectangular chamber to form a uniform flow channel (0.025 cm in height, 1.0 cm in width, and 5.0 cm in length) created by sandwiching a silicon gasket between the glass slide (with ECs) and a chamber glass plate. Laminar shear flow with 12 dyn/cm^2 wall shear stress through the channel was generated by the hydrostatic pressure difference between two reservoirs. The oscillatory flow is composed of a low level of mean flow (wall shear stress = 0.5 dyn/cm^2) supplied by a hydrostatic flow system to provide the basal nutrient and oxygen delivery, and a superimposed sinusoidal oscillation using a piston pump with a frequency of 1 Hz and a peak-to-peak amplitude of ±4 dyn/cm^2.

During the flow experiments, the system was kept at 37 °C in a constant temperature hood, and the circulating medium (DMEM supplemented with 10% FBS) was ventilated with humidified 5% CO_2–95% air to maintain pH at 7.4.

Finite element methods. The 3D traction stress vector, $\boldsymbol{\sigma}$, was computed from the measured 3D substrate deformation field by solving a boundary value problem under the assumption of isotropic and elastic material properties based on our previous study, and the boundary conditions (BCs) determined from the displacement field (1). This problem was solved with the finite element method (FEM). 3D stresses (forces per area) and strain energy density (strain energy per area) were determined from the 3D stress tensor field computed by FEM. Strain energy density is defined as the work stored in the substrate per area and is calculated as

$$\mathrm{SE} = \frac{1}{2}\int \boldsymbol{\sigma} \cdot \mathbf{u}\,\mathrm{ds}, \qquad \textbf{[S3]}$$

where $\mathbf{u}$ is the 3D displacement vector on the surface of the substrate. For FE analysis, the hexahedron (brick) type element, which has eight nodes at the corners and eight Gauss integration points inside, was used. ABAQUS (Dassault Systemes), a commercial software package for FE analysis, was used for this numerical calculation.

Statistics. We used non-parametric box plot to depict groups of numerical data through seven number summaries. Statistical properties of data shown in box plot are as follows: median (center line), filled area (95% significance rage of median), box (25/75% percentile), and whisker (1.5 Lower quartile/1.5 Upper quartile). Outliers were removed from the plot. The Wilcoxon rank-sum test was used to test significance between two groups, and Kruskal-Wallis followed by multi-comparison test was used to test significance among multiple groups (8).

Simulation of boundary effects in 3D-TFM. Two simulation experiments were designed to determine the applicability of 3D-TFM to confluent cell monolayers. The substrate was assumed to have linear elastic material properties with a Young's Modulus of 3.63 kPa and a Poisson's ratio of 0.3. The thickness of the substrate was assumed to be 40 μm following the real experimental conditions.

In the first simulation, we investigated the spatial decay of substrate deformation as a function of distance from a cell. To mimic a situation of cells with forces applied outside the field of view (Fig. S2*A*, *Left*, 110 μm × 144 μm, dotted rectangle), eight pairs of 1-nN forces (Fig. S2*A*, *Left*, black arrows) are placed outside of the domain with the same microscopic field of view. Each pair is used to simulate a balanced artificial cell. The separation of a pair of forces (or size of a cell) is about 10 μm, and the distance between a point force and the field of view is also 10 μm. Deformation fields resulting from the eight artificial cells are shown in

Fig. S2*A* (*Right*). The substrate deformation was examined along the section line (dotted white lines) in vertical (L1) and horizontal (L2) directions. In both cases, the substrate deformation decays markedly with distance such that they decrease to less than 5% at one distance of cell length, i.e., at about a cell size (Fig. S2*B*).

We can conclude from these results that, if we quantify the substrate deformation within the boundary of this characteristic value $\delta\,(\text{distance/cell size}) = 1.0$ away from the outside cells, most of the deformations induced by adjacent cells can be excluded with a limited error of 5%. The maximum value at the peak was chosen as 100%.

We designed another simulation to estimate how a cell located at the center of the microscopic field of view is affected by the cells located outside of the field of view (Fig. S2*C*). In 3D-TFM, we can observe displacements only in the microscopic field of view and use this field for the calculation of traction stress (**TS**) and strain energy density (**SE**). To mimic this situation in simulation, **TS** is computed by solving partial differential equations using the displacement field only in the 110 μm × 144 μm region (solid green lines in Fig. S2*C*, *Center*) as boundary conditions (BCs). The case with outer cells (w/ OC, Fig. S2*C*, *Right top*) is compared with the case without outer cells (w/o OC, Fig. S2*C*, *Right bottom*). **TS** and **SE** are examined along red dotted line (w/ OC) and white dotted line (w/o OC) in vertical (L1) and horizontal (L2) directions, respectively. In both cases, the magnitudes of traction stresses (TS_{mag}) w/ OC and w/o OC are very close (Fig. S2*D*). The differences between the two are less than 8% (Fig. S2*E*). The maximum value in the field of view is used as 100%. Differences in SEmag are again negligible (Fig. S2*F* and *G*). These results show that "outer cells" did not affect the computation of traction stresses.

The results from these two simulations indicate that the effects of the traction stresses induced by cells outside the field of view are insignificant on the computed traction stress and strain energy of the cells in the monolayer being studied if data points beyond 1-cell distance are excluded. In our study, junctional tension (**JT**) and intracellular tension (**IT**) of cell monolayers are computed from traction stresses only within the area 10-μm from the edges (Fig. 1*F* and *I*, white lines).

Direction of cell–cell tensions. We have investigated the relations of the orientation of **JT** to that of the cell-cell junction and to the magnitude of **JT** (Fig. S3*A* and *B*, respectively). The schematic inset in Fig. S3*A* shows the angle θ of **JT** to cell–cell junction, which was determined from end-to-end points of intercellular junctions. The value reflecting orthogonality ($|90 - \theta|$, a small value indicates that the junction tension is more orthogonal to section line) is significantly different between 2 Cells (26°) and M Cells (41°). As a corollary, the relationships between the perpendicular ($JT_{\perp}$) and parallel ($JT_{||}$) components of **JT** are different between these two group, with $JT_{\perp} > JT_{||}$ in 2 Cells and $JT_{\perp} \approx JT_{||}$ in M Cells (Fig. S3*B*), and the ratio $JT_{\perp}/JT_{||}$ is larger in 2 Cells than M Cells (Fig. S3*C*). In the 2-Cell case, each cell transmits tensions to only its single partner; in the M-Cell case, however, each cell transmits tensions with all surrounding neighbors. Thus, reduced orthogonality between **JT** and cell–cell junction indicates that EC monolayers experience higher parallel **JT**, due to the effect of neighbor cells.

Direction of intracellular tension under flow. Direction as well as magnitude of IT_{xy} were investigated (Fig. S4 schematic) at sections perpendicular to flow (Fig. S4*A*, *Left*) and parallel to flow (Fig. S4*A*, *Right*). Under LS with time, orthogonality did not change with time at $\alpha = 0°$, but it is markedly reduced at $\alpha = 90°$. After 24 h of LS, both perpendicular ($IT_{\perp}$) and parallel ($IT_{||}$) components of IT_{xy} are increased at $\alpha = 90°$ (Fig. S4*D*, *Left*), but only parallel components is increased at $\alpha = 0°$ (Fig. S4*D*, *Right*). These results were reaffirmed by the ratio $IT_{\perp}/IT_{||}$ (Fig. S4*G*).

Under OS and control condition, the direction of intracellular tensions did not show significant change with time (Fig. S4*B* and *C*); $IT_{\perp}$ and $IT_{||}$ also did not change significantly with time (Fig. S4*E* and *F*), nor did the ratio $IT_{\perp}/IT_{||}$ (Fig. S4*H* and *I*).

These results indicate that flow shear with a clear direction modulates the orthogonality between intracellular tension and intracellular section line.

1. Hur SS, Zhao Y, Li YS, Botvinick E, Chien S (2009) Live cells exert 3D traction forces on their substrata. *Cell Mol Bioeng* 2:425–436.
2. Li C, Hu Z, Li Y (1993) Poisson's ratio in polymer gels near the phase-transition point. *Phys Rev E Stat Phys Plasmas Fluids Relat Interdiscip Topics* 48:603–606.
3. del Alamo JC, et al. (2010) 3D forces exerted by migrating amoeboid cells. *Biophys J* 98:427a.
4. Chiu JJ, Chien S (2011) Effects of disturbed flow on vascular endothelium: pathophysiological basis and clinical perspectives. *Physiol Rev* 91:327–387.
5. del Alamo JC, Norwich GN, Li YS, Lasheras JC, Chien S (2008) Anisotropic rheology and directional mechanotransduction in vascular endothelial cells. *Proc Natl Acad Sci USA* 105:15411–15416.
6. Frangos JA, Eskin SG, McIntire LV, Ives CL (1985) Flow effects on prostacyclin production by cultured human endothelial cells. *Science* 227:1477–1479.
7. Wang N, et al. (2006) Shear stress regulation of Kruppel-like factor 2 expression is flow pattern-specific. *Biochem Biophys Res Commun* 341:1244–1251.
8. Hollander M, Wolfe DA (1999) *Nonparametric Statistical Methods* (Wiley, New York) 2nd Ed, pp xiv, 787 p

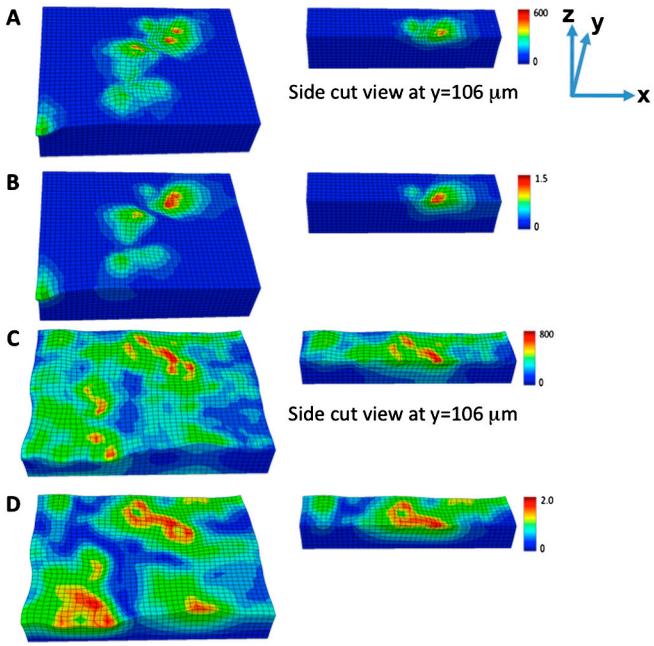

Fig. S1. Diagonal and side-cut views of reconstructed stress and displacement fields in 3D. (*A*) Stress magnitude (von Mises) of a pair of ECs in contact. Left figure shows diagonal view and right figure shows side-cut view at y = 106 μm. Unit of pseudocolor bar is Pa. (*B*) Displacement magnitude of a pair of ECs in contact. Left figure shows diagonal view and right figure shows side-cut view at y = 106 μm. Unit of pseudocolor bar is μm. (*C*) Stress magnitude (von Mises) of confluent EC monolayer. Left figure shows diagonal view and right figure shows side-cut view at y = 106 μm. Unit of pseudocolor bar is Pa. (*D*) Displacement magnitude of confluent EC monolayer. Left figure shows diagonal view and right figure shows side-cut view at y = 106 μm. Unit of pseudocolor bar is μm. Cells are located on the top of xy plane (Fig. 1*A* and *B*).

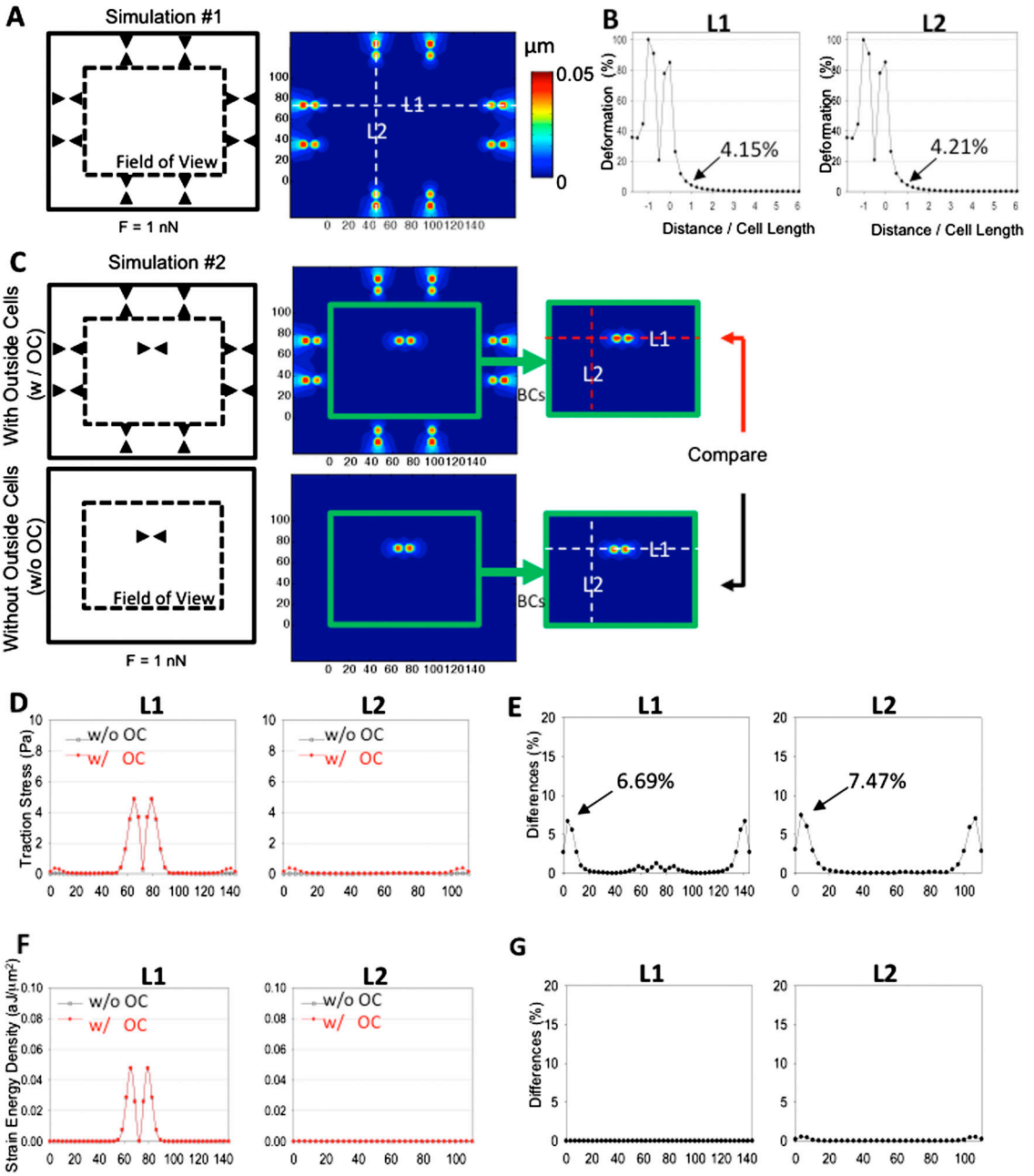

Fig. S2. Simulations showing rapid decay of substrate deformation so that the effect of cells located outside of field of view is negligible 10 μm away. (*A, Left*) Schematic of simulation #1 showing the decay of substrate deformation. A pair of black arrows indicates a cell. Each arrow represents a force of 1 nN. Black dotted lines indicate microscopic field of view with a size of 144 × 110 μm. (*B, Left*) Decay of deformation field normalized by the maximum along section line L1. (*B, Right*) Decay of deformation field normalized by the maximum along section line L2. (*B, Right*) Decay of deformation field normalized by maximum along section line L2. (*C, Left*) Schematic of simulation #2 comparing with outside cells (*Top*) and without outside cells (*Bottom*). A pair of black arrows indicate a cell. Each arrow represents a force of 1 nN. Black dotted lines indicate microscopic field of view with a size of 144 × 110 μm. (*C, Middle*) Contour of deformation field calculated with outer boundary. White dotted line indicates section line. (*C, Right*) Contour of deformation field computed from BCs (deformation within microscopic field of view). Red dotted lines indicate section lines for with outer boundary in horizontal direction along L1 and vertical direction along L2. White dotted lines indicate section lines without outer boundary in horizontal direction along L1 and vertical direction along L2. (*D, Left*) Comparison of traction stresses between with outside cells (red) and without outside cells (black) in L1. (*D, Right*) Comparison of traction stresses between with outside cells (red) and without outside cells (black) along section line L2. (*E, Left*) Difference of traction stresses between with outside cells and without outside cells along section line L1. (*E, Right*) Difference of traction stresses between with outside cells and without outside cells along section line L2. (*F, Left*) Comparison of strain energy densities between with outside cells (red) and without outside cells (black) in L1. (*F, Right*) Comparison of strain energy densities between with outside cells (red) and without outside cells (black) in L2. (*G, Left*) Difference of strain energy density between with outside cells and without outside cells along section line L1. (*G, Right*) Difference of strain energy density between with outside cells and without outside cells along section line L2.

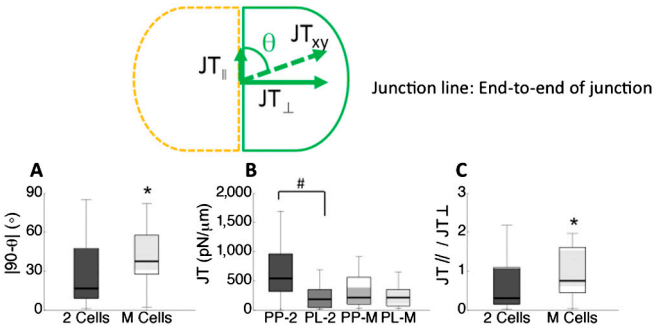

Fig. S3. Orthogonality of cell–cell tension to junctional section line. (*A*) Angle of cell–cell tension to junction. Junction line is determined from end-to-end points of the cell–cell junction. (*B*) Perpendicular and parallel components of cell–cell tensions. PP-2 indicates perpendicular component of two ECs. PL-2 indicates parallel components of two ECs. PP-M indicate perpendicular component of EC monolayers. PL-M indicates parallel components of EC monolayers. (*C*) Ratio of parallel to perpendicular components of cell-cell tensions. * P < 0.05, # P < 0.001 The numbers of data are 20 and 24 for two ECs and EC monolayers, respectively.

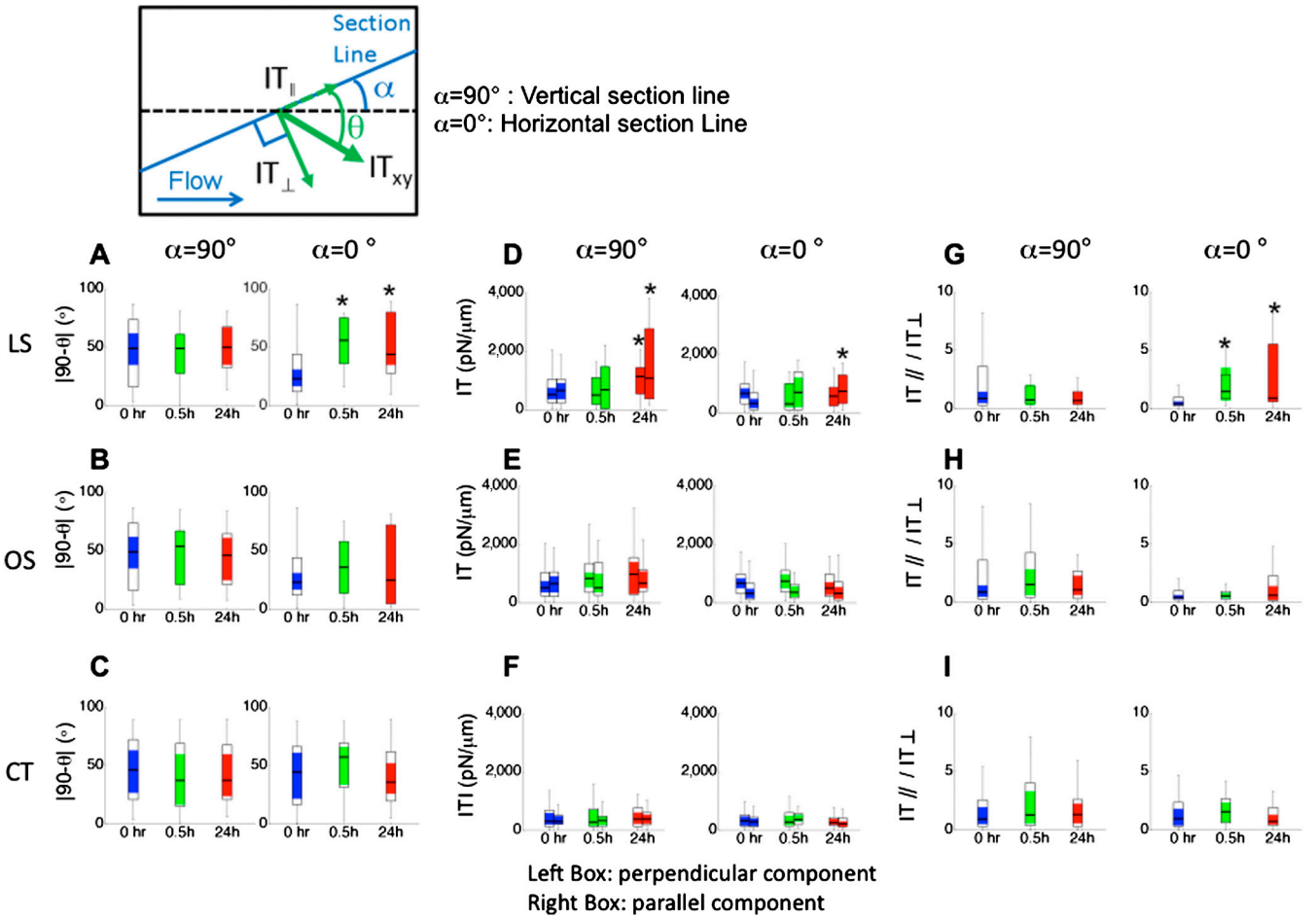

Fig. S4. Orthogonality of intracellular tension to intracellular section line by different flow shear (*A, Left*) Angle change of intracellular tensions to section lines under laminar shear at intracellular section lines in vertical directions ($\alpha = 90°$). (*A, Right*) Angle change of intracellular tensions to section lines under laminar shear at intracellular section lines in horizontal directions ($\alpha = 0°$). (*B, Left*) Angle change of intracellular tensions to section lines under oscillatory shear at intracellular section lines in vertical directions ($\alpha = 90°$). (*B, Right*) Angle change of intracellular tensions to section lines under oscillatory shear at intracellular section lines in horizontal directions ($\alpha = 0°$). (*C, Left*) Angle change of intracellular tensions to section lines under no shear (control) at intracellular section lines in vertical directions ($\alpha = 90°$). (*C, Right*) Angle change of intracellular tensions to section lines under no shear (control) at intracellular section lines in horizontal directions ($\alpha = 0°$). (*D, Left*) Intracellular tensions under laminar shear at intracellular section lines in vertical directions ($\alpha = 90°$). (*D, Right*) Intracellular tensions under laminar shear at intracellular section lines in horizontal directions ($\alpha = 0°$). (*E, Left*) Intracellular tensions under oscillatory shear at intracellular section lines in vertical directions ($\alpha = 90°$). (*E, Right*) Intracellular tensions under oscillatory shear at intracellular section lines in horizontal directions ($\alpha = 0°$). (*F, Left*) Intracellular tensions under no shear (control) at intracellular section lines in vertical directions ($\alpha = 90°$). (*F, Right*) Intracellular tensions under no shear (control) at intracellular section lines in horizontal directions ($\alpha = 0°$). (*G, Left*) Ratio of parallel to perpendicular components of intracellular tension under laminar shear at intracellular section lines in vertical directions ($\alpha = 90°$). (*G, Right*) Ratio of parallel to perpendicular components of intracellular tension under laminar shear at intracellular section lines in horizontal directions ($\alpha = 0°$). (*H, Left*) Ratio of parallel to perpendicular components of intracellular tension under oscillatory shear at intracellular section lines in vertical directions ($\alpha = 90°$). (*H, Right*) Ratio of parallel to perpendicular components of intracellular tension under oscillatory shear at intracellular section lines in horizontal directions ($\alpha = 0°$). (*I, Left*) Ratio of parallel to perpendicular compo-

nents of intracellular tension under no shear (control) at intracellular section lines in vertical directions ($\alpha = 90°$). (*I*, *Right*) Ratio of parallel to perpendicular components of intracellular tension under no shear (control) at intracellular section lines in horizontal directions ($\alpha = 0°$). (*D–F*) Left box indicates perpendicular component and right box indicates parallel component of intracellular tension. LS, OS, and CT denote laminar shear, oscillatory shear, and control (no flow), respectively. Colors of blue, green and red indicate 0, 0.5, and 24 h, respectively. The numbers of data samples are 14, 36, and 57 for laminar shear, oscillatory shear, and control, respectively.